The Spherical-Actuator-Magnet Manipulator: A Permanent-Magnet Robotic End-Effector

Samuel E. Wright, Arthur W. Mahoney, *Member, IEEE*, Katie M. Popek, *Member, IEEE*,
and Jake J. Abbott, *Member, IEEE*

Abstract—A variety of magnetic devices can be manipulated remotely using a single permanent "actuator" magnet positioned in space by a robotic manipulator. This paper describes the spherical-actuator-magnet manipulator (SAMM), which is designed to replace or augment the singularity-prone spherical wrist used by prior permanent-magnet manipulation systems. The SAMM uses three omniwheels to enable holonomic control of the heading of its magnet's dipole and to enable its magnet to be rotated continuously about any axis of rotation. The SAMM performs closed-loop control of its dipole's heading using field measurements obtained from Hall-effect sensors as feedback, combined with modeled dynamics, using an extended Kalman filter. We describe the operation and construction of the SAMM, develop and characterize controllers for the SAMM's spherical magnet, and demonstrate remote actuation of an untethered magnetic device in a lumen using the SAMM.

Index Terms—Magnetic dipole, magnetic manipulation, medical robotics, microrobotics, spherical mechanism.

I. INTRODUCTION

THIS paper describes the spherical-actuator-magnet manipulator (SAMM), which is a mechatronic device housing a solid uniformly magnetized spherical permanent magnet that is intended to be used as the "actuator magnet" in a magnetic-manipulation system. The SAMM is designed to be used as an end-effector mounted to the tool frame of a robotic manipulator that is used to *position* the spherical magnetic in space (see Fig. 1). The SAMM enables holonomic singularity-free control
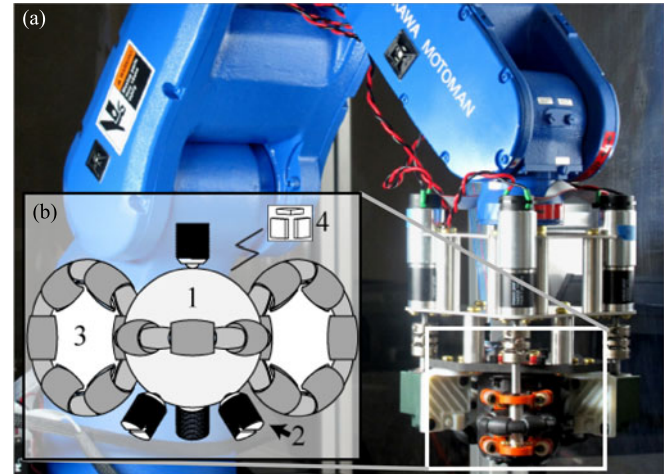

Fig. 1. (a) SAMM prototype as the end-effector of a robotic manipulator. (b) Concept diagram illustrating the spherical magnet (1), which is prevented from translating by four constraints (2) that create a rolling form-closure. Three omniwheels (3) whose axes of rotation span $\mathbb{R}^3$ contact the magnet and cause it to rotate as desired. Magnetic-field sensors (4) measure the magnet's dipole moment to be used for closed-loop control of the dipole's heading (i.e., 2-DOF orientation).

of the *orientation* of its spherical magnet, as well as continuous rotation of its magnet about arbitrary axes of rotation. The SAMM was designed so as to remove kinematic limitations encountered in prior permanent-magnet manipulation systems. This distal surface of the SAMM is designed to be smooth and free of moving parts, so that the spherical magnet can be placed very close to the magnetic device that it is trying to actuate or manipulate.

Two prior works in our lab motivated the development of the SAMM. The ability to control a screw-like untethered magnetic device (UMD) in a lumen using a single *rotating* permanent magnet as the actuation source, in a task reminiscent of active capsule endoscopy in the intestines, was described in [1]. The results of [1] enable the actuator magnet to be placed in any position relative to the UMD, provided a specific position-dependent actuator-magnet rotation axis is established. In the experimental results of [1], the actuator magnet was rotated by a single DC motor that was rigidly mounted to the tool frame of an industrial six-degree-of-freedom (6-DOF) robotic manipulator. In that setup, the rotation axis of the actuator magnet was fixed with respect to the tool frame of the robotic manipulator. Such a setup is capable of placing the actuator magnet with the

correct rotation axis to guide a UMD through relatively simple trajectories. However, when tasked with navigating a UMD through tortuous paths (e.g., the small intestines), the physical constraints of the robotic manipulator (i.e., joint limits and singularities) limit how the UMD can be actuated, and limit the workspace.

The effects of manipulator limitations on UMD actuation were also observed and were characterized in [2], where a single, *nonrotating* permanent magnet was used to levitate a semibuoyant magnetic capsule with 5-DOF (3-DOF position and 2-DOF heading) control in a task reminiscent of capsule endoscopy in the stomach. Kinematic singularities and workspace limitations were identified as the primary limiting factors to dexterous manipulation. To mitigate the effect of singularities, the authors introduced a control method that sacrificed control authority over the capsule's heading in order to maintain 3-DOF control over the capsule's position when the manipulator nears a kinematic singularity.

The SAMM has no joint limits or kinematic singularities by design. This is made possible by using three omniwheels to drive the SAMM's spherical magnet. An omniwheel is a common mechanism that incorporates small rollers that permit controlled rotation about the omniwheel's rotation axis and free rotation about the two orthogonal axes. Designing the three omniwheel rotation axes to be linearly independent enables any instantaneous magnet rotation axis to be achieved. By making the magnet's axis of rotation continuously variable, irrespective of the robotic manipulator used to position the SAMM, the kinematic singularities of the robotic manipulator can be avoided, and the robotic manipulator is free to position the actuator magnet optimally for manipulation. The SAMM will also enable robotic manipulators with less than 6-DOF to be considered for use in magnetic manipulation (e.g., a simple 3-DOF gantry system or SCARA robot). With singularity-free orientation control of its spherical magnet, the SAMM can be used to solve the problems found in both of the projects described above, and has the potential to be used for the remote actuation of a variety of magnetic devices that have been previously developed for minimally invasive medicine, including both UMDs [1], [3]–[11], and tethered magnetic devices such as catheters and cochlear-implant electrode arrays [12], [13].

There are several reasons for choosing a magnet of spherical geometry. First, being of constant radius, it is simple to maintain form-closure regardless of the magnet's orientation, enabling it to be easily incorporated into a physical device. Second, a spherical magnet makes the best use of available space in the sense that it fully fills the volume of its bounding sphere with magnetic material to maximize the strength of the magnetic dipole. Third, the field of a spherical permanent magnet is theoretically perfectly fit by the simple point-dipole model [14], [15], which enables analytic tools to be accurately applied. Finally, a spherical body has no principal directions of inertia, giving it isotropic dynamic properties, which is particularly valuable during continuous rotation.

Our SAMM design was inspired by prior "ballbot" systems, in which a robot balances itself atop a sphere (e.g., a bowling ball) [16], [17]. With ballbots, only the instantaneous angular velocity of the ball is important for control, and the ball's orientation is not measured [18] (i.e., there is no preferred "north pole" of a bowling ball). However, for remote magnetic manipulation, knowledge of the magnet's dipole heading is critical since it determines the field applied to the actuated magnetic device and how the device is controlled. Therefore, the SAMM includes a magnetic-field sensor system to estimate the spherical-magnet's dipole heading. The SAMM is fundamentally different—in terms of design, control, and end use—from spherical motors, which use electromagnetic stator coils to orient a permanent-magnet spherical rotor (see [19]).

We use the term "heading" since the dipole's magnitude is constant and known, and we are only interested in the 2-DOF pointing orientation of the dipole rather than the full 3-DOF orientation of the sphere. This is because the field generated by a spherical permanent magnet is radially symmetric about its dipole axis, so rotations about the dipole axis neither result in a change in the magnetic field to the remote device being actuated nor to the sensors measuring the field.

In this paper, we expand the results of [20] in the following ways.

1) A Kalman filter is presented that estimates the spherical magnet's dipole heading and angular velocity by synthesizing sensor feedback and modeled dynamics.
2) We describe our mechanical approach to keep the omniwheels in contact with the spherical magnet despite nonidealities.
3) We present a new "pointing mode" controller that solely controls the spherical magnet's dipole heading.
4) We present an improved version of the "rotating mode" controller.
5) We describe how to calibrate the magnetic-field sensors used to measure the spherical magnet's heading, which substantially improves the accuracy of the estimation of the spherical magnet's dipole heading.
6) We present two additional experiments that assess the performance of the controllers we present herein.

II. VELOCITY KINEMATICS AND INVERSE KINEMATICS

We follow a convention where scalars are denoted by lower case standard font (e.g., c), vectors by lower case bold font (e.g., $\mathbf{x}$), and matrices by capital bold font (e.g., $\mathbf{M}$). The "hat" symbol denotes a unit-length vector (e.g., $\hat{\mathbf{x}}$).

For some desired angular velocity $\boldsymbol{\omega}_\mathbf{m} \in \mathbb{R}^3$ of the spherical magnet, the necessary omniwheel rotation speeds must be determined. Let the unit-length vectors $\hat{\mathbf{d}}_1$, $\hat{\mathbf{d}}_2$, and $\hat{\mathbf{d}}_3$ point from the magnet's center to the contact points where the three omniwheels touch the magnet (see Fig. 2). We assume that the omniwheel axes $\hat{\mathbf{a}}_1$, $\hat{\mathbf{a}}_2$, and $\hat{\mathbf{a}}_3$ are perpendicular to $\hat{\mathbf{d}}_1$, $\hat{\mathbf{d}}_2$, and $\hat{\mathbf{d}}_3$, respectively, and assume that there is no slip between the omniwheels and the magnet. Given a magnet angular velocity $\boldsymbol{\omega}_\mathbf{m}$, the surface velocity of the magnet at the ith omniwheel–magnet contact point is given as

$$\mathbf{u}_i = r_m \boldsymbol{\omega}_\mathbf{m} \times \hat{\mathbf{d}}_i \qquad (1)$$
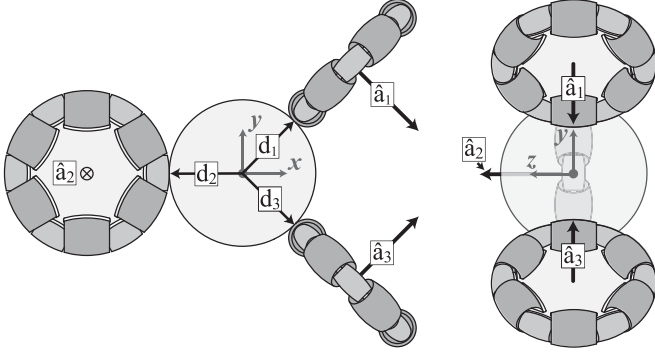
where r_m is the radius of the magnet.

Fig. 2. Two orthogonal views of the SAMM's omniwheel configuration are shown. The vectors $\hat{\mathbf{a}}_1$, $\hat{\mathbf{a}}_2$, and $\hat{\mathbf{a}}_3$ are the omniwheel rotation axes, and $\hat{\mathbf{d}}_1$, $\hat{\mathbf{d}}_2$, and $\hat{\mathbf{d}}_3$ point from the magnet center to the corresponding omniwheel contact point. The depicted coordinate system is used throughout this paper.

The components of $\mathbf{u}_1$, $\mathbf{u}_2$, and $\mathbf{u}_3$ parallel to the respective omniwheel axes are transferred directly into rotation of the omniwheel rollers, and cause no rotation of the omniwheels themselves. All other components of $\mathbf{u}_1$, $\mathbf{u}_2$, and $\mathbf{u}_3$ cause each omniwheel to rotate with scalar rotation speeds ω_{a1}, ω_{a2}, and ω_{a3}, respectively. The component direction of $\mathbf{u}_i$ that causes the ith omniwheel to rotate about its axis is given as

$$\hat{\mathbf{q}}_i = \hat{\mathbf{d}}_i \times \hat{\mathbf{a}}_i. \tag{2}$$

Under the assumption of no-slip, the projection of $\mathbf{u}_1$, $\mathbf{u}_2$, and $\mathbf{u}_3$ onto the directions $\hat{\mathbf{q}}_1$, $\hat{\mathbf{q}}_2$, and $\hat{\mathbf{q}}_3$, respectively, must be mapped to the scalar rotation speeds of each omniwheel by the reciprocal of the omniwheels' radii (denoted by r_w, as we assume identical omniwheels) as

$$\omega_{ai} = \frac{1}{r_w}\hat{\mathbf{q}}_i^\mathsf{T}\mathbf{u}_i = \frac{r_m}{r_w}\hat{\mathbf{a}}_i^\mathsf{T}\{\hat{\mathbf{d}}_i\}^2\,\boldsymbol{\omega}_{\mathbf{m}} \tag{3}$$

where $\{\hat{\mathbf{d}}_i\} \in so(3)$ is the skew-symmetric matrix form of the cross-product operation.

All three omniwheel rotation speeds can be packed into the vector $\boldsymbol{\omega}_{\mathbf{a}}$ and related to the spherical magnet angular velocity $\boldsymbol{\omega}_{\mathbf{m}}$, in matrix form, as

$$\boldsymbol{\omega}_{\mathbf{a}} = \begin{bmatrix} \omega_{a1} \\ \omega_{a2} \\ \omega_{a3} \end{bmatrix} = \frac{r_m}{r_w} \begin{bmatrix} \hat{\mathbf{a}}_1^\mathsf{T}\{\hat{\mathbf{d}}_1\}^2 \\ \hat{\mathbf{a}}_2^\mathsf{T}\{\hat{\mathbf{d}}_2\}^2 \\ \hat{\mathbf{a}}_3^\mathsf{T}\{\hat{\mathbf{d}}_3\}^2 \end{bmatrix} \boldsymbol{\omega}_{\mathbf{m}}. \tag{4}$$

Due to the assumption that $\hat{\mathbf{a}}_i$ is perpendicular to $\hat{\mathbf{d}}_i$, (4) can be simplified to

$$\boldsymbol{\omega}_{\mathbf{a}} = -\frac{r_m}{r_w} \begin{bmatrix} \hat{\mathbf{a}}_1^\mathsf{T} \\ \hat{\mathbf{a}}_2^\mathsf{T} \\ \hat{\mathbf{a}}_3^\mathsf{T} \end{bmatrix} \boldsymbol{\omega}_{\mathbf{m}} = \eta\mathbf{A}^\mathsf{T}\boldsymbol{\omega}_{\mathbf{m}} \tag{5}$$

where $\eta = -r_m/r_w$ is the gear ratio from the omniwheels to the sphere (with the negative sign indicating the change in rotation direction from the omniwheels to the magnet), and $\mathbf{A} = \begin{bmatrix} \hat{\mathbf{a}}_1 & \hat{\mathbf{a}}_2 & \hat{\mathbf{a}}_3 \end{bmatrix}$.

The omniwheel axes and positioning must be designed such that matrix $\mathbf{A}$ has full rank, otherwise there will exist a di-

rection of $\boldsymbol{\omega}_{\mathbf{m}}$ that cannot be achieved with any selection of omniwheel rotation speeds. Although linear independence of the columns of $\mathbf{A}$ is a sufficient condition mathematically, in practice the columns should be designed to be as close to mutually orthogonal as possible. Otherwise, some desired $\boldsymbol{\omega}_{\mathbf{m}}$ will require an unnecessarily, and possibly unachievably, fast omniwheel rotation speed. We designed our system so that $\hat{\mathbf{a}}_1$, $\hat{\mathbf{a}}_2$, and $\hat{\mathbf{a}}_3$ are mutually orthogonal and arranged as shown in Fig. 2. This counter-opposed configuration results in the omniwheel axes: $\hat{\mathbf{a}}_1 = [\sqrt{2}/2\ \sqrt{2}/2\ 0]^\mathsf{T}$, $\hat{\mathbf{a}}_2 = [0\ 0\ (-1)]^\mathsf{T}$, and $\hat{\mathbf{a}}_3 = [\sqrt{2}/2\ (-\sqrt{2}/2)\ 0]^\mathsf{T}$. Other feasible omniwheel arrangements are possible [21].

III. SYSTEM DYNAMICS

The net applied torque $\boldsymbol{\tau}_{\mathbf{m}}$ on the actuator magnet is related to the magnet's instantaneous angular velocity $\boldsymbol{\omega}_{\mathbf{m}}$ and angular acceleration $\dot{\boldsymbol{\omega}}_{\mathbf{m}}$ by

$$\boldsymbol{\tau}_{\mathbf{m}} = \mathbf{J}\dot{\boldsymbol{\omega}}_{\mathbf{m}} + \mathbf{B}(\boldsymbol{\omega}_{\mathbf{m}})\boldsymbol{\omega}_{\mathbf{m}} + \mathbf{c}(\boldsymbol{\omega}_{\mathbf{m}}, \boldsymbol{\tau}_{\mathbf{m}}) \tag{6}$$

where the manipulator's rotational inertia matrix is denoted by $\mathbf{J} \in \mathbb{R}^{3\times3}$, the viscous friction matrix is denoted by $\mathbf{B}(\boldsymbol{\omega}_{\mathbf{m}}) \in \mathbb{R}^{3\times3}$, and the Coulomb friction is denoted by $\mathbf{c}(\boldsymbol{\omega}_{\mathbf{m}}, \boldsymbol{\tau}_{\mathbf{m}}) \in \mathbb{R}^3$.

The rotational inertia matrix $\mathbf{J}$ is the combination of the inertia due to the spherical magnet $\mathbf{J}_{\mathbf{m}}$ and the inertia due to the motors and omniwheels $\mathbf{J}_{\mathbf{w}}$:

$$\mathbf{J} = \mathbf{J}_{\mathbf{m}} + \eta^2\mathbf{J}_{\mathbf{w}} = \frac{2}{5}m_m r_m^2 \mathbf{I}_{\mathbf{3}} + \eta^2\left(\frac{1}{2}m_w r_w^2 + j_{\mathrm{mot}}\right)\mathbf{I}_{\mathbf{3}} \tag{7}$$

where the gear ratio η is defined in Section II, m_m is the mass of the spherical magnet, and r_m is its radius. The rotational inertia of each omniwheel includes the omniwheel's inertia (approximated as a rotating disk with radius r_w and mass m_w) and the corresponding driving motor's inertia j_{mot} (this term includes the motor's rotor inertia reflected through any gearing in the motor, as seen at the output shaft). Matrix $\mathbf{I}_{\mathbf{3}} \in \mathbb{R}^{3\times3}$ is the identity matrix.

We have observed viscous and Coulomb friction effects [22] that are asymmetric. The viscous friction matrix $\mathbf{B}(\boldsymbol{\omega}_{\mathbf{m}})$ is modeled as $\mathbf{B} = \mathrm{diag}(B_1, B_2, B_3)$, where the coefficients B_i are determined according to the sign of the corresponding terms of $\boldsymbol{\omega}_{\mathbf{m}}$:

$$B_i = \begin{cases} B_i^+ & : \omega_{\mathrm{m},i} > 0 \\ B_i^- & : \omega_{\mathrm{m},i} < 0. \end{cases} \tag{8}$$

The Coulomb friction term $\mathbf{c}(\boldsymbol{\omega}_{\mathbf{m}}, \boldsymbol{\tau}_{\mathbf{m}})$, which models static friction, is defined as

$$c_i = \begin{cases} \tau_i & : \omega_{\mathrm{m},i} = 0 \text{ and } c_i^- \le \tau_{\mathrm{m},i} \le c_i^+ \\ c_i^+ & : \omega_{\mathrm{m},i} = 0 \text{ and } \tau_{\mathrm{m},i} > c_i^+ \\ c_i^- & : \omega_{\mathrm{m},i} = 0 \text{ and } \tau_{\mathrm{m},i} < c_i^- \\ c_i^+ & : \omega_{\mathrm{m},i} > 0 \\ c_i^- & : \omega_{\mathrm{m},i} < 0. \end{cases} \tag{9}$$

Note that similarly to how magnet angular velocity $\boldsymbol{\omega}_{\mathbf{m}}$ is mapped to motor angular velocity $\boldsymbol{\omega}_{\mathbf{a}}$ via (5), the magnet torque $\boldsymbol{\tau}_{\mathbf{m}}$ is mapped to motor torque $\boldsymbol{\tau}_{\mathbf{a}}$ through $\mathbf{A}^\mathsf{T}$, but with the

inverse of the gear ratio:

$$\boldsymbol{\tau_a} = \frac{1}{\eta} \mathbf{A}^\mathsf{T} \boldsymbol{\tau_m}. \tag{10}$$

IV. SENSING THE MAGNET'S DIPOLE MOMENT

The dipole moment of the magnetic body (denoted by the vector $\mathbf{m}$) is the vector from the south to north poles of the magnet. Methods of magnetic manipulation using a single permanent magnet require the magnet's dipole moment to be specifically directed and thus known. The dipole moment $\mathbf{m}$ of the SAMM's magnet can be determined by measuring the magnetic field $\mathbf{h}$ that it generates in space.

One approach to measuring the magnetic field uses Hall-effect sensors, which measure the component of the field in the direction normal to (i.e., passing through) the sensor's face. We assume the general case of n Hall-effect sensors. Let each sensor be positioned in space such that the vectors $\mathbf{p}_1$ through $\mathbf{p}_n$, in units of meters, measure each sensor's position relative to the spherical magnet's center, and let $\hat{\mathbf{v}}_1$ through $\hat{\mathbf{v}}_n$ be unit-magnitude vectors that describe the directions that are sensed by each sensor; all vectors are expressed in the same frame as $\mathbf{m}$. Let the magnetic field at each sensor position be denoted by $\mathbf{h}_1$ through $\mathbf{h}_n$, in units $\text{A} \cdot \text{m}^{-1}$. The measured component of the field produced by the ith sensor is denoted with the scalar s_i and is given by

$$s_i = \hat{\mathbf{v}}_i^\mathsf{T} \mathbf{h}_i. \tag{11}$$

The magnetic field $\mathbf{h}_i$, at each sensor position $\mathbf{p}_i$, can be predicted with the point-dipole model

$$\mathbf{h}_i = \frac{1}{4\pi \left\| \mathbf{p}_i \right\|^3} \left(3\hat{\mathbf{p}}_i \hat{\mathbf{p}}_i^\mathsf{T} - \mathbf{I_3} \right) \mathbf{m} = \mathbf{H}_i \mathbf{m} \tag{12}$$

which exactly predicts the field produced by a spherical permanent magnet [14], [15]. For all other geometries, it is an approximation that becomes more accurate with increasing distance [23].

Substituting (12) into (11) produces an expression relating the magnet's dipole moment $\mathbf{m}$ to each of the n sensor measurements, which can be aggregated into the following matrix equation:

$$\mathbf{s} = \begin{bmatrix} s_1 \\ \vdots \\ s_n \end{bmatrix} = \begin{bmatrix} \hat{\mathbf{v}}_1^\mathsf{T} \mathbf{H}_1 \\ \vdots \\ \hat{\mathbf{v}}_n^\mathsf{T} \mathbf{H}_n \end{bmatrix} \mathbf{m} = \mathbf{S}\mathbf{m}. \tag{13}$$

The $n \times 3$ constant matrix $\mathbf{S}$ encapsulates the complete geometric description of the sensor arrangement, as it pertains to estimating $\mathbf{m}$. If the matrix $\mathbf{S}$ has full column rank, then a solution for the dipole moment $\mathbf{m}$ can be found as

$$\mathbf{m} = \mathbf{S}^\dagger \mathbf{s} \tag{14}$$

where $\mathbf{S}^\dagger = \mathbf{V}\mathbf{\Sigma}^\dagger\mathbf{U}^\mathsf{T}$ is the Moore–Penrose pseudoinverse of $\mathbf{S}$, using the singular-value decomposition $\mathbf{S} = \mathbf{U}\mathbf{\Sigma}\mathbf{V}^\mathsf{T}$, where the columns of $\mathbf{U}$ and $\mathbf{V}$ are the output and input singular vectors of $\mathbf{S}$, respectively, $\mathbf{\Sigma}$ contains the singular values of $\mathbf{S}$ on the main diagonal and zeros elsewhere, and $\mathbf{\Sigma}^\dagger$ is the transpose of $\mathbf{\Sigma}$ in which the nonzero singular values have been replaced by
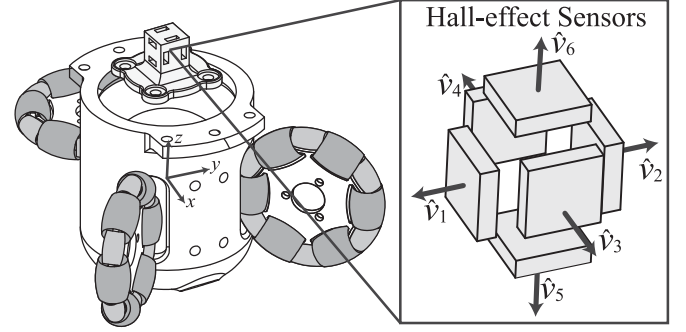

Fig. 3. Sensor cluster comprising six Hall-effect sensors, mounted directly above the housing, with coordinate system and numbering convention shown.

their reciprocals [24]. The matrix $\mathbf{S}$ should be made to have full column rank by using at least three Hall-effect sensors and appropriately selecting the positions ($\mathbf{p}_i$) and directions ($\hat{\mathbf{v}}_i$) of each sensor. When $n > 3$, (14) provides the best estimate of $\mathbf{m}$ in a least-squares sense. Along with making $\mathbf{S}$ full rank, the sensors should also be ideally arranged to minimize the variance of the measured dipole moment by decreasing the singular values of $\mathbf{S}$. Note that the constant matrix $\mathbf{S}^\dagger$ can be calculated offline.

For our system, we designed a sensor cluster comprising six 1-DOF Allegro A1302 Hall-effect sensors that are arranged on the surface of a cube and positioned in close proximity to each other. The sensor cluster is mounted to the SAMM, as shown in Fig. 3. In addition to being a space free from moving parts, this location ensures that magnetic-field disturbances in the workspace below the SAMM (e.g., from the magnet of a device being manipulated by the SAMM) have a minimal impact on the estimation of the SAMM magnet's dipole heading. The sensors, which have a sensitivity of 13 mV/mT, utilize their full output-voltage range without saturation. We describe the poses of the sensors quantitatively in Section VIII. Other sensor arrangements are considered in [21].

V. STATE ESTIMATION

Although (14) provides an instantaneous measurement of the magnet's dipole, filtering incorporates knowledge of the manipulator's dynamics to reduce the effects of sensor noise. We have chosen to implement the hybrid extended Kalman filter (EKF) [25], which linearizes the system's nonlinear dynamic and observation equations about the current predicted state before employing the Kalman filter algorithm, and which uses continuous-time equations to model the system's dynamics but performs system observation in discrete time.

A. Review of the Hybrid EKF

We briefly review the hybrid EKF as described in [25] for completeness. The hybrid implementation (otherwise known as the discrete-time implementation) of the EKF allows for the state $\mathbf{x}(t)$ and state estimate covariance to transition continuously according to the models

$$\dot{\mathbf{x}}(t) = \mathbf{f}\big(\mathbf{x}(t), \mathbf{u}(t)\big) + \mathbf{w}(t) \tag{15}$$

$$\dot{\mathbf{P}}(t) = \mathbf{F}(t)\mathbf{P}(t) + \mathbf{P}(t)\mathbf{F}(t)^\mathsf{T} + \mathbf{Q} \qquad (16)$$

respectively, where $\mathbf{f}\big(\mathbf{x}(t), \mathbf{u}(t)\big)$ models the system's dynamics given the input $\mathbf{u}(t)$ and process noise $\mathbf{w}(t) \sim \mathcal{N}(0, \mathbf{Q})$, and the linearization matrix $\mathbf{F}(t)$ is given as

$$\mathbf{F}(t) = \left.\frac{\partial \mathbf{f}}{\partial \mathbf{x}}\right|_{\bar{\mathbf{x}}(t), \mathbf{u}(t)}. \qquad (17)$$

Discrete measurements at the jth time step are modeled as

$$\mathbf{z}_j = \mathbf{g}(\mathbf{x}_j) + \mathbf{v}_j \qquad (18)$$

where $\mathbf{x}_j = \mathbf{x}(t_j)$ and $\mathbf{v}_j \sim \mathcal{N}(0, \mathbf{R})$ is zero-mean measurement noise that is uncorrelated in time.

1) Predict: An *a priori* state estimate $\mathbf{x}_{j|j-1}$ and covariance $\mathbf{p}_{j|j-1}$ can be recursively predicted from the *a posteriori* estimate at the previous time step t_{j-1} by integrating (15) and (16) using a zero-order hold on the system inputs $\mathbf{u}(t)$:

$$\mathbf{x}_{j|j-1} = \mathbf{x}_{j-1|j-1} + \int_{t_{j-1}}^{t_j} \mathbf{f}(\mathbf{x}(t), \mathbf{u}(t_{j-1}))dt \qquad (19)$$

$$\mathbf{P}_{j|j-1} = \mathbf{P}_{j-1|j-1} + \int_{t_{j-1}}^{t_j} \dot{\mathbf{P}}(t)dt. \qquad (20)$$

2) Update: The *a priori* estimate is updated to become the *a posteriori* estimate by performing a Kalman update with sensor observations. The Kalman gain $\mathbf{K}_j$ is computed using the *a priori* covariance, the linearization of the observation model $\mathbf{g}$, and the covariance of observation noise $\mathbf{R}$ as

$$\mathbf{K}_j = \mathbf{P}_{j|j-1}\mathbf{G}_j^\mathsf{T}(\mathbf{G}_j\mathbf{P}_{j|j-1}\mathbf{G}_j^T + \mathbf{R})^{-1} \qquad (21)$$

where $\mathbf{G}_j$ is given as

$$\mathbf{G}_j = \left.\frac{\partial \mathbf{g}}{\partial \mathbf{x}}\right|_{\bar{\mathbf{x}}_{j|j-1}}. \qquad (22)$$

The Kalman update is calculated by comparing the actual sensor observation $\mathbf{z}$ with the predicted observation $\mathbf{g}(\mathbf{x}_{j|j-1})$:

$$\mathbf{x}_{j|j} = \mathbf{x}_{j|j-1} + \mathbf{K}_j\big(\mathbf{z}_j - \mathbf{g}(\mathbf{x}_{j|j-1})\big) \qquad (23)$$

$$\mathbf{P}_{j|j} = \big(\mathbf{I} - \mathbf{K}_j\mathbf{G}_j\big)\mathbf{P}_{j|j-1}. \qquad (24)$$

B. Implementing the Hybrid EKF

The SAMM state is represented as the vector

$$\mathbf{x} = \begin{bmatrix} \hat{\mathbf{m}} \\ \boldsymbol{\omega}_\mathbf{m} \end{bmatrix} \in \mathbb{S}^2 \times \mathbb{R}^3 \qquad (25)$$

packed with the unit-length dipole moment heading $\hat{\mathbf{m}} \in \mathbb{S}^2$ and the magnet's angular velocity $\boldsymbol{\omega}_\mathbf{m} \in \mathbb{R}^3$.

The continuous-time evolution of the SAMM state and covariances are given by (15) and (16), where $\mathbf{f}(\mathbf{x}, \mathbf{u})$ is

$$\mathbf{f}(\mathbf{x}, \mathbf{u}) = \begin{bmatrix} \boldsymbol{\omega}_\mathbf{m} \times \hat{\mathbf{m}} \\ \mathbf{J}^{-1}\big(\boldsymbol{\tau}_\mathbf{m} - \mathbf{B}(\boldsymbol{\omega}_\mathbf{m})\boldsymbol{\omega}_\mathbf{m} - \mathbf{c}\left(\boldsymbol{\omega}_\mathbf{m}, \boldsymbol{\tau}_\mathbf{m}\right)\big) \end{bmatrix} \qquad (26)$$

where $\mathbf{u} = \boldsymbol{\tau}_\mathbf{m}$ is the system input, and $\mathbf{F}$ is calculated as

$$\mathbf{F} = \frac{\partial \mathbf{f}}{\partial \mathbf{x}} = \begin{bmatrix} \{\boldsymbol{\omega}_\mathbf{m}\} & -\{\hat{\mathbf{m}}\} \\ \mathbf{0} & -\mathbf{J}^{-1}\mathbf{B}(\boldsymbol{\omega}_\mathbf{m}) \end{bmatrix}. \qquad (27)$$

Note that the Coulomb friction term $\mathbf{c}(\boldsymbol{\omega}_\mathbf{m}, \boldsymbol{\tau}_\mathbf{m})$ does not vary with $\hat{\mathbf{m}}$ or $\boldsymbol{\omega}_\mathbf{m}$ when $\boldsymbol{\omega}_\mathbf{m} \neq \mathbf{0}$, additionally both $\mathbf{B}(\boldsymbol{\omega}_\mathbf{m})$ and $\mathbf{c}(\boldsymbol{\omega}_\mathbf{m}, \boldsymbol{\tau}_\mathbf{m})$ are not differentiable when $\boldsymbol{\omega}_\mathbf{m} = \mathbf{0}$ but we neglect this issue for simplicity since $\boldsymbol{\omega}_\mathbf{m}$ is rarely $\mathbf{0}$.

Observations are performed in discrete-time using the Hall-sensor system described in Section IV, which estimates the dipole moment $\mathbf{m}$, and using measurements of the magnet's angular velocity obtained by differentiating the motor encoder position and using (5). The observation model is structured as

$$\mathbf{z} = \mathbf{g}(\mathbf{x}) = \begin{bmatrix} \mathbf{S}\,\|\mathbf{m}\| & \mathbf{0} \\ \mathbf{0} & \mathbf{I_3} \end{bmatrix}\mathbf{x} \qquad (28)$$

where $\mathbf{S}$ is the Hall-sensor matrix defined in (13). The observation model $\mathbf{g}(\mathbf{x})$ is then linearized as

$$\mathbf{G} = \frac{\partial \mathbf{g}}{\partial \mathbf{x}} = \begin{bmatrix} \mathbf{S}\,\|\mathbf{m}\| & \mathbf{0} \\ \mathbf{0} & \mathbf{I_3} \end{bmatrix}. \qquad (29)$$

VI. CONTROL

The SAMM has two modes of operation: *pointing* and *rotating*. Examples of where the pointing mode would be useful include any tasks requiring quasistatic magnetic fields, such as the actuation of an endoscopic capsule in the stomach [2], a magnet-tipped catheter [12], or a magnet-tipped cochlear-implant electrode array [13]. Examples of where the rotating mode would be useful include any task where a rotating magnetic field is fundamental to the actuation strategy, such as rolling UMDs along a surface [6]–[8], swimming through a fluid or crawling through a lumen via helical propulsion [9], [10], [26]–[28], or screwing through soft tissue [11].

Subsequent to [20] and [21], additional testing revealed that the original rotating-mode controller was not stable for all rotation axes at speeds greater than 1 Hz. The improved controller presented here provides stable rotation for all axes and speeds tested (up to 3 Hz); this maximum is due to hardware limitations. In this updated implementation, custom pointing-mode and rotating-mode controllers output a necessary magnet angular velocity $\boldsymbol{\sigma}$, which is mapped to the motor-space by the transmission matrix $\mathbf{A}$. The desired motor velocity of each omniwheel is input to its corresponding Maxon motor controller (ESCON 36/2), which provides onboard closed-loop velocity control and is tuned specifically for its wheel. We found a simple proportional controller was sufficient for both our pointing- and rotating-mode controllers because of the closed-loop velocity control.

A. Pointing-Mode Controller

The pointing-mode controller governs the *heading* of the actuator-magnet dipole moment $\hat{\mathbf{m}}$ to align along a desired heading $\hat{\mathbf{m}}_\mathbf{des} \in \mathbb{S}^2$. A proportional heading-control scheme is employed using the Kalman filter's estimate of the dipole moment $\hat{\hat{\mathbf{m}}}$. In order to drive $\hat{\hat{\mathbf{m}}}$ toward $\hat{\mathbf{m}}_\mathbf{des}$, the heading's restoration error vector $\mathbf{e}$ is computed as

$$\mathbf{e} = \theta\hat{\mathbf{n}} \qquad (30)$$

where θ is the angle between $\hat{\hat{\mathbf{m}}}$ and $\hat{\mathbf{m}}_\mathbf{des}$, and the vector $\hat{\mathbf{n}}$ lies in the direction of $\hat{\hat{\mathbf{m}}} \times \hat{\mathbf{m}}_\mathbf{des}$. The angular velocity $\boldsymbol{\sigma}$

commanded to the individual motors' velocity controllers is computed as

$$\boldsymbol{\sigma} = k_p \mathbf{e} \tag{31}$$

where k_p is the proportional gain.

B. Rotating-Mode Controller

The purpose of the rotating-mode controller is to generate continuous rotation of the actuator-magnet dipole with some desired angular velocity $\boldsymbol{\omega}_{\mathbf{m,des}}$, with the dipole orthogonal to $\boldsymbol{\omega}_{\mathbf{m,des}}$, without any concern for the phase of the dipole within the cycle. Similar to the previous rotating-mode controller [20], [21], the updated version simultaneously employs two control laws: a feedforward angular-velocity subcontroller that rotates $\hat{\mathbf{m}}$ about a desired angular velocity vector $\boldsymbol{\omega}_{\mathbf{m,des}}$, and a proportional heading subcontroller to drive $\hat{\mathbf{m}}$ to the plane *orthogonal* to $\boldsymbol{\omega}_{\mathbf{m,des}}$ with control effort given by $\boldsymbol{\sigma}_{\perp}$. The two control laws are combined to form the total output angular velocity

$$\boldsymbol{\sigma} = \boldsymbol{\omega}_{\mathbf{m,des}} + \boldsymbol{\sigma}_{\perp} \tag{32}$$

which is sent to the motors' velocity controllers. Note that the terms $\boldsymbol{\omega}_{\mathbf{m,des}}$ and $\boldsymbol{\sigma}_{\perp}$ are always orthogonal to each other and hence they do not fight each other in the control effort.

Control effort in the direction orthogonal to $\boldsymbol{\omega}_{\mathbf{m,des}}$ is computed as

$$\boldsymbol{\sigma}_{\perp} = k_{p\perp} \mathbf{e}_{\perp}. \tag{33}$$

The rotation-plane restoration vector $\mathbf{e}_{\perp}$ used to drive $\hat{\mathbf{m}}$ to the desired rotation plane is found as

$$\mathbf{e}_{\perp} = \hat{\mathbf{m}} \times \widehat{\mathbf{\Pi}\hat{\mathbf{m}}} \tag{34}$$

where

$$\mathbf{\Pi} = \left(\mathbf{I_3} - \hat{\boldsymbol{\omega}}_{\mathbf{m,des}} \hat{\boldsymbol{\omega}}_{\mathbf{m,des}}^{\mathsf{T}} \right) \tag{35}$$

$\mathbf{\Pi}$ is a projection operator onto the plane defined by the normal vector $\boldsymbol{\omega}_{\mathbf{m,des}}$, and the rightmost term in the cross product in (34) represents the normalized projection of $\hat{\mathbf{m}}$ onto the desired plane. $\mathbf{e}_{\perp}$ was chosen to connote "error"; it does approximate the true angular error at small angles, but will have a magnitude that is smaller than the angular error (i.e., sinusoidal in angular error) at larger values, preventing large misalignments from resulting in abrupt accelerations and undesirable slipping between the omniwheels and the spherical magnet. Unlike in the pointing mode, the cross product can be used in place of error because the deviation of $\hat{\mathbf{m}}$ from the desired rotation plane is at most 90°, so the magnitude of $\mathbf{e}_{\perp}$ is guaranteed to be monotonic with angular error. Equation (34) breaks down when $\hat{\mathbf{m}}$ is parallel to $\hat{\boldsymbol{\omega}}_{\mathbf{m,des}}$. In this case, the error between $\hat{\mathbf{m}}$ and the desired rotation plane is 90°, and any direction of motion will decrease the error from the plane equally well, so we calculate the restoration vector as $\mathbf{e}_{\perp} = \hat{\mathbf{m}} \times \widehat{\mathbf{\Pi}\boldsymbol{\xi}}$, where $\boldsymbol{\xi}$ is an arbitrary vector not parallel to $\hat{\mathbf{m}}$ (in our implementation of the controller it is randomly generated).
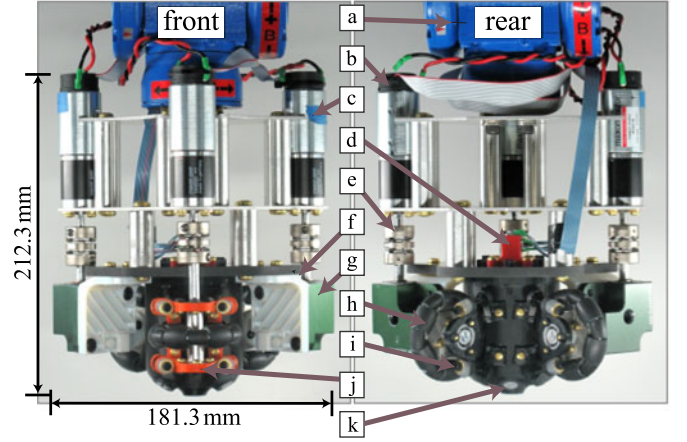

Fig. 4. Prototype SAMM shown mounted to the tool frame (a) of robotic manipulator. Encoders (b) measure the gearmotors' (c) position. The cluster of Hall-effect sensors (d) measures the spherical magnet's dipole. Power is transmitted through aluminum helical shaft couplings (e) to omniwheel axles or 90° gearboxes (g), which pivot for omniwheel compliance (f). Omniwheels (h) are tensioned to the spherical magnet through adjustable spring-tensioned pillow blocks (i), whose tension can be manually tuned through adjustment screws (j). Adjustable ball-roller-tip set-screws (k) create rolling form-closure for the spherical magnet.

VII. PROTOTYPE IMPLEMENTATION

Our prototype SAMM is shown in Fig. 4. The magnetic body is a 50.8-mm-diameter, Grade-N42, spherical permanent magnet with a dipole strength of 66.0 A·m². The field produced by the spherical magnet, which is accurately modeled by the point-dipole model (12), is strong in close proximity. During the design process, we eliminated soft-magnetic components (e.g., steel, iron, etc.) from the SAMM where possible, since soft-magnetic material near the magnet becomes magnetized under applied fields and would then exert an undesirable magnetic torque and force on the spherical magnet. For example, we chose to use plastic screws (instead of steel) to hold the SAMM mechanism together. Where it was not possible to eliminate soft-magnetic material (e.g., the gearmotors), we designed the SAMM mechanism in a way that placed soft-magnetic material as far from the spherical magnet as possible, where the fields are weakest and the soft-magnetic material would be magnetized the least.

Additionally, time-varying magnetic fields (caused by rotating the magnet) induce eddy currents in nearby electrically conductive material; these circulating currents create their own magnetic field, resulting in drag on the magnet. When possible, we used nonconductive material for components that are close to the spherical magnet (where the fields are largest and eddy currents would be highest). For example, the magnet enclosure is milled out of black Nylon and the ball-roller-tip set-screws that touch the magnet are made out of polyacetal and ceramic.

The form-closure constraints [see Figs. 1(b) and 4(k)] that allow only rotation of the spherical magnet are implemented with a set of four ball-roller-tipped precision set-screws. The smallest number of such constraints needed to guarantee form-closure is four, with three constraints whose contact points on

the magnet do not form a hemispherical great circle on the actuator magnet and a fourth constraint contacting normal to the plane established by the first three. Housed inside the tip of the set-screw is a freely rotating 5.56-mm ball that is supported by 1.50-mm subrollers. The set-screws are threaded into the housing of the mechanism so that they constrain the magnet in its desired position with minimal perceptible play when installed flush with reference bosses on the exterior of the housing. The body of the set-screws are polyacetal Misumi set-screws (BCS-BJJ) with the ball-tips and subrollers replaced with ceramic parts, making each set-screw nonmagnetic and nonconductive.

The housing of the device resembles a cylindrical structure with a hemisphere at one end where three of the four form-closure constraints are mounted. The housing is constructed out of nonconductive ABS plastic to mitigate eddy currents. The omniwheels contact the magnet through windows in the cylindrical body. The omniwheels are arranged in a counter-opposed configuration, which results in the normal forces from each omniwheel being supported by the other omniwheels, which mutually increases their traction, unlike other potential configurations where the normal forces are supported by the form-closure constraints resulting in higher rotating friction.

The custom omniwheels [see Fig. 4(h)] are based on designs described in [29] and [16], and provide nearly continuous contact with the magnet. Each omniwheel roller contains dual ceramic ball bearings for minimal friction under load, as well as a soft neoprene heat-shrink sleeve on the surface for increased traction. It is important to maximize traction to maximize achievable acceleration and bandwidth. The omniwheels are constructed with fully nonmagnetic components. Some components are conductive, but their volume is small and effects from eddy currents are not noticeable. When fully assembled, the major diameter of each omniwheel is 58.2 mm.

The omniwheels are driven by three Maxon RE-max 29 gearmotors [see Fig. 4(c)], which have a 24:1 gear ratio and 512 CPT encoders [see Fig. 4(b)], mounted with their shafts in parallel. The torques applied to omniwheel axes $\hat{a}_1$ and $\hat{a}_3$ are redirected via 90° gearboxes [see Fig. 4(g)]; the torque applied to omniwheel axis $\hat{a}_2$ is transmitted without an additional gearbox. The 90° gearboxes comprise nylon gears mounted to aluminum shafts and are supported by dual acetal ball bearings inside an aluminum case, making the 90° gearboxes entirely nonmagnetic. The gearmotors are connected to the respective drive shafts by aluminum helical couplings [see Fig. 4(e)].

Due to irregularities that exist in the omniwheels' circularity caused by gaps between omniwheel rollers and unintentional eccentricity in the mechanical mounting, we found in our prototype development that it was beneficial to include mechanical compliance to maintain robust contact between the omniwheels and the magnet. The compliance should compensate for irregularities without altering the torque transmission matrix $\mathbf{A}$, keeping $\hat{a}_i$ constant and perpendicular to $\hat{d}_i$ through its range of travel. Our SAMM prototype employs two different approaches. In the case of omniwheels 1 and 3 [see Fig. 2(f)], 1-DOF rotary compliance is employed as illustrated in Fig. 5(a). The rotary axes lie parallel to the respective omniwheel axes. The 90° gearboxes make the rotary axis perpendicular to the respective
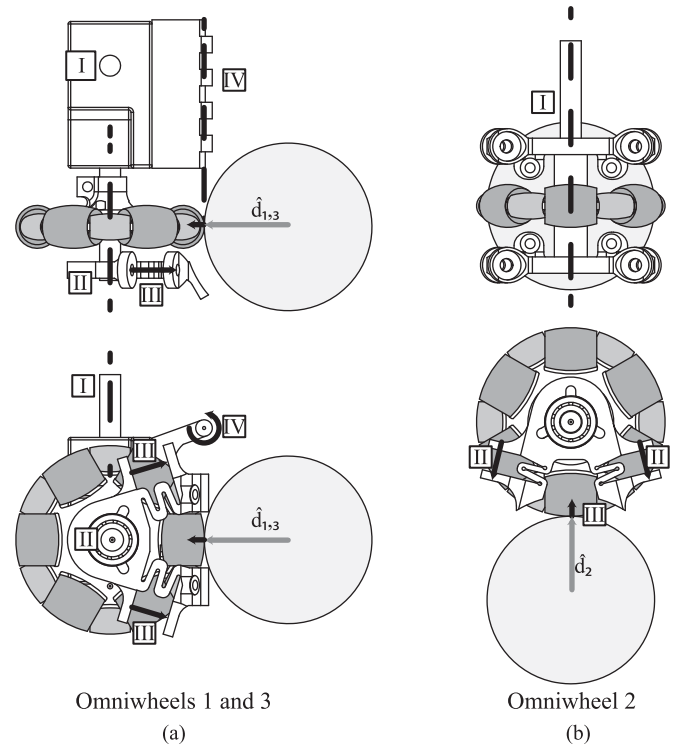

Omniwheels 1 and 3

(a)

Omniwheel 2

(b)

Fig. 5. Compliance at the omniwheel–magnet interface axes $\hat{a}_i$. (a) Omniwheels 1 and 3 are depicted. The motor's axis (I) is transmitted through the 90° gearbox to the omniwheel's axis (II). Adjustable spring-tensioned pillow blocks provide force (III) between the omniwheel and the magnet, creating compliance (IV) locally parallel with $\hat{d}_i$. (b) Omniwheel 2 is depicted. The motor's axis and the omniwheel's axis are coaxial, but the remainder of the design is similar.

motor axis, which decouples the direction of compliance from the direction of motor torque transmission (avoiding potential problems related to binding or traction loss). Tension is applied to the omniwheel assemblies by adjustable spring-tensioned pillow blocks constructed of three-dimensional (3-D)-printed ABS plastic with cutouts revealing serpentine-shaped springs, which are reinforced with a silicone compression spring whose tension can be increased or decreased by tightening or loosening an adjustment screw [see Fig. 4(j)]. For omniwheel 2, approximate straight-line motion is formed utilizing two adjustable spring-tensioned pillow blocks, similar to those used on axes 1 and 3, to tension the omniwheel directly onto the magnet in the direction $\hat{d}_2$, illustrated in Fig. 5(b). Although the motion is not strictly constrained to $\hat{d}_2$, we have found that the deviation is insignificant.

The Hall-effect sensor cluster depicted in Fig. 3 is fabricated by 3-D printing a housing from ABS plastic with slots in which the Hall-effect sensors are inserted and affixed with adhesive. The nominal positions and sensing directions of the sensors are given in Table I. However, as we describe in Section VIII, the values were updated using a calibration procedure.

Our SAMM prototype is intended to be mounted as the end-effector of a robotic manipulator [see Fig. 1(a)]. In this configuration, the SAMM can be positioned so that its distal surface [the hemispherical side where three of the four set-screws are

TABLE I
HALL-EFFECT SENSOR PARAMETERS FOR SAMM PROTOTYPE

Sensor	Nominal Position Vector $\mathbf{p}_i^\mathsf{T}$ (mm)	Nominal Sensing Direction $\mathbf{v}_i^\mathsf{T}$	Calibrated Position Vector $\mathbf{p}_i^\mathsf{T}$ (mm)	Calibrated Sensing Direction $\mathbf{v}_i^\mathsf{T}$
1	$[\,0 \quad 0 \quad 51.0\,]$	$[\,0 \quad 0 \quad 1\,]$	$[\,-0.611 \quad 0.112 \quad 50.8\,]$	$[\,0.00520 \quad -0.0604 \quad 0.998\,]$
2	$[\,0 \quad 0 \quad 58.5\,]$	$[\,0 \quad 0 \quad 1\,]$	$[\,-0.953 \quad -0.101 \quad 59.0\,]$	$[\,0.0126 \quad 0.0527 \quad 0.999\,]$
3	$[\,3.75 \quad 0 \quad 54.7\,]$	$[\,1 \quad 0 \quad 0\,]$	$[\,4.38 \quad 0.0474 \quad 55.3\,]$	$[\,0.995 \quad -0.0969 \quad -0.0148\,]$
4	$[\,-3.75 \quad 0 \quad 54.7\,]$	$[\,1 \quad 0 \quad 0\,]$	$[\,-4.03 \quad 0.407 \quad 55.9\,]$	$[\,0.987 \quad -0.133 \quad -0.0948\,]$
5	$[\,0 \quad 3.75 \quad 54.7\,]$	$[\,0 \quad 1 \quad 0\,]$	$[\,-0.0210 \quad 3.78 \quad 55.2\,]$	$[\,0.0453 \quad 0.998 \quad 0.0359\,]$
6	$[\,0 \quad -3.75 \quad 54.7\,]$	$[\,0 \quad 1 \quad 0\,]$	$[\,0.0768 \quad -3.52 \quad 54.6\,]$	$[\,0.0894 \quad 0.996 \quad -0.0388\,]$

Note: See Section IV for parameter definitions.

located, as shown in Fig. 4(k)], which is streamlined and free of moving parts, is presented to the manipulation workspace (e.g., a human body), reducing the risk of collisions or damage to the moving SAMM components and enabling the actuator magnet to be positioned close to the remote magnetic device being manipulated in order to maximize the strength of the applied magnetic field. In our case, we use a 6-DOF manipulator, but a 3-DOF Cartesian manipulator would be sufficient due to the 3-DOF of the SAMM.

VIII. EXPERIMENTATION

All experiments were performed with the SAMM mounted to a 6-DOF Yaskawa Motoman robotic manipulator, which is housed in an enclosure to mitigate environmental disturbances. The SAMM was always oriented "vertically," as depicted in Fig. 1. The control system and data recording were implemented in C++ and using a Sensoray 626 PCI DAQ card. The control system is designed in a multithreaded structure with the control loop, the Kalman-estimator loop, and the SAMM I/O loop all operating at 200 Hz.

A. Parameter Estimation

1) Coulomb and Viscous Friction: Friction in the SAMM was estimated using a directional Coulomb-plus-viscous friction model described in Section III. The friction parameters were experimentally obtained by driving the motors at open-loop velocities ranging, in discrete increments, from 0 to 2π rad/s. Each increment lasted for 30 s while the resulting motor torque ($\boldsymbol{\tau}_\mathbf{a}$) and sensed motor angular velocity ($\boldsymbol{\omega}_\mathbf{a}$) were recorded at a rate of 20 Hz. The motor torque is automatically computed by the Maxon motor controllers that drive the three motors. Lines were fit to the positive- and negative-velocity data [21], using least squares, whose *y*-intercept and slope corresponding to the Coulomb friction ($\mathbf{c}$) and viscous friction ($\mathbf{B}$), respectively, were found to be

$$\mathbf{B}^+ = \mathrm{diag}\,(0.0001, 0.0014, 0.0001)\,\mathrm{N \cdot s/rad},$$

$$\mathbf{B}^- = \mathrm{diag}\,(0.00001, 0.0014, 0.0005)\,\mathrm{N \cdot s/rad},$$

$$\mathbf{c}^+ = [0.0632\ \ 0.0411\ \ 0.0436]^\mathsf{T}\mathrm{N},$$

$$\mathbf{c}^- = [-0.0455\ \ -0.0330\ \ -0.0723]^\mathsf{T}\mathrm{N}.$$

2) Sensor Noise: Noise from each of the sensors is modeled with the observation covariance matrix $\mathbf{R}$ described in Section V. The submatrix of $\mathbf{R}$ that corresponds to the Hall-sensor covariance is directly estimated by removing the spherical magnet from the SAMM and reading the idle sensor values to determine their intrinsic noise. The submatrix corresponding to the angular-velocity-measurement covariance is measured by recording the covariance of the angular-velocity sensor values with the motors driven open-loop with a constant input (which we assume results in approximately constant motor angular velocity). In both cases, sensor data are collected at a rate of 20 Hz for a duration of 10 min. The covariances and means of the first 50% of the data were compared to the final 50% to verify that the estimation had converged and enough data were collected. Each sensor was independently evaluated for a dc offset, which is then removed in implementation to ensure that the noise measured by each sensor is zero-mean. Note that we assume the Hall-sensor measurements to be independent from the angular-velocity measurements, which causes the off-diagonal terms of $\mathbf{R}$ to be zero. The observation covariance measured and implemented in our SAMM prototype is given as

$$\mathbf{R} = \mathrm{diag}(2.9, 2.9, 2.9, 2.8, 2.9, 2.8, 6.0, 6.0, 6.0) \cdot 10^{-3}$$

where the units of the top-left 6×6 submatrix of $\mathbf{R}$ is mT^2, and the bottom-right 3×3 submatrix of $\mathbf{R}$ have units $\mathrm{rad}^2/\mathrm{s}^2$.

3) Process Noise: Process noise, represented by the covariance matrix $\mathbf{Q}$, is difficult to measure directly, so we experimentally tuned the process-noise covariance to produce desirable tracking performance:

$$\mathbf{Q} = \mathrm{diag}(0.002, 0.002, 0.002, 2.0, 2.0, 2.0).$$

The top-left 3×3 submatrix, which corresponds to heading uncertainty, was set to the value of δ (0.001 in the prototype SAMM) multiplied by the value used in the bottom-right 3×3 submatrix, which in turn corresponds to the magnet's angular-velocities uncertainty represented by a constant multiplied by an identity matrix; the rationale behind this choice is that dipole heading is estimated by integrating angular velocity over one time step, so angular-velocity error is mapped to heading error in a predictable way. This constraint reduced the tuning search to a 1-DOF search. Similar to the structure of $\mathbf{R}$, the off-diagonal terms of $\mathbf{Q}$ have been set to zero as we assume all of the states to be independent. The units of $\mathbf{Q}$ correspond to the units of the

state, where the upper left block matrix denotes the covariance of the dipole heading (which is a unitless heading on the unit-sphere), and the lower right block matrix is the covariance of the dipole's angular velocity measured in rad^2/s^2.

4) Hall-Effect Sensor Calibration: Discrepancies in the Hall-effect sensors' nominal design values (see Table I) will lead to errors when estimating the magnet's dipole heading. To address this problem, the 5-DOF pose of each of the SAMM's six Hall-effect sensors was calibrated, utilizing an external three-axis Metrolab THM1176-LF gaussmeter mounted below the SAMM. To find the position directly below the magnet, a manual gradient-ascent search was employed by moving the SAMM in a horizontal plane to find the location that resulted in the maximum field component in the vertical direction, which is known from (12) to occur directly below the magnet if the dipole is oriented vertically. The search was accomplished by alternately moving the SAMM in a 1 mm grid pattern and manually adjusting the omniwheels to maximize the vertical field component measured. Upon convergence, we knew the magnet was located directly above the gaussmeter, and that it was oriented vertically. The distance of the dipole above the sensor is then calculated using (12) and knowledge of the dipole's magnitude.

Next, with the SAMM's position stationary, 26 random dipole headings were generated by randomly moving the omniwheels between each trial. For each dipole heading, the SAMM's Hall-effect sensor data and the gaussmeter data were collected. With a known and constant position vector, we used the gaussmeter readings to approximate the true heading $\hat{\mathbf{m}}$ of the dipole for each of the 26 tests, using the Levenberg–Marquardt least-squares algorithm in MATLAB to minimize $\|\mathbf{h}_e - \mathbf{h}_m\|^2$, where $\mathbf{h}_m$ is the 3-D field measured by the gaussmeter, and $\mathbf{h}_e$ is the field estimated by (12) using the current estimate of $\hat{\mathbf{m}}$.

Next, using our dataset with known dipole headings, a similar method was utilized to estimate the 5-DOF pose of each Hall-effect sensor independently, using the complete dataset. The point-dipole equation is projected onto the measuring axis of each sensor, $\hat{\mathbf{v}}_i$, to estimate the scalar magnetic field at each sensor position as in (11). Starting from the initial nominal estimates in Table I, the unit vector $\hat{\mathbf{v}}_i$ and the position vector $\mathbf{p}_i$ are approximated using a constrained nonlinear least-squares algorithm to minimize $\|\mathbf{s_e} - \mathbf{s_m}\|^2$, where $\mathbf{s_m}$ is an array of scalar field measurements by an individual sensor at each of the 26 dipole headings, and $\mathbf{s_e}$ contains the corresponding values estimated by (11) using the current estimates of $\hat{\mathbf{v}}_i$ and $\mathbf{p}_i$. To average sensor noise, 100 measurements from each of the 26 dipole headings were recorded, for a total of 2600 measurements per sensor.

Finally, this calibration process was tested by comparing an additional ten random dipole headings measured by the gaussmeter with those reported by the SAMM sensors. The error across these ten tests was $1.5° \pm 0.6°$ (mean $\pm$ standard deviation). For comparison, using the nominal values from Table I in (14) would have resulted in an error across these ten tests of $5.3° \pm 2.6°$. Note that in our calibration procedure, we assumed that the Hall-effect sensors' sensitivities were accurately provided by the manufacturer. This assumption will lead to a small error in the calibrated position $\mathbf{p}_i$ in Table I (increased/decreased

sensitivity would translate the sensor's position estimate radially inward/outward from the dipole), but the resulting estimated dipole heading will be the same.

B. Controller Tuning

This section describes the gain tuning for both controllers introduced in Section VI. In order to implement the proportional pointing-mode and "orthogonal" rotating-mode controllers, which are both effectively forms of heading regulation, we must select the respective controller gains. The Ziegler–Nichols tuning method is a heuristic-based approach to tuning such controllers [30]. The method involves creating a proportional controller and slowly increasing its gain until marginal stability is observed (i.e., when the experimentally observed oscillations are neither decreasing nor increasing over time). This gain defines the "ultimate gain" k_u, and the period of the resulting oscillations defines the "ultimate period" t_u. These identified parameters, which are specific to the SAMM for a given magnitude of step input (since the SAMM is not a linear system), are used to determine all relevant gains. The tuning parameters were experimentally found to be $k_u = 21.0 \text{ s}^{-1}$ and $t_u = 0.65 \text{ s}$, when tuning for a step-input magnitude of 5°. The Ziegler–Nichols formulation for a proportional controller, which sets $k_p = 0.5 \, k_u = 10.5 \text{ s}^{-1}$, was found to generate desirable performance in both the pointing and rotating modes.

C. Performance Demonstrations

1) Pointing Mode: To test the pointing mode, we performed a Monte Carlo experiment where the SAMM was initialized with the dipole moment $\hat{\mathbf{m}}$ at a random heading and then commanded to go to a new desired heading in a random direction with an angular change of 5°, 90°, or 175°. In total, 150 random trials were performed, with 50 trials for each magnitude of angular change. Each random heading was held constant for 10 s. The root-mean-square (RMS) error was measured during the last 5 s of each trial. Across the 150 trials, the RMS error mean $\pm$ standard deviation was $0.2° \pm 0.1°$.

During the Monte Carlo experiment, we measured the time required to converge to each random desired heading for each magnitude of angular change. The convergence time t_c was defined as the time to reach and stay within $1.0°$ of the desired heading. Fig. 6(a) shows the mean and standard deviation of t_c as a function of the step input θ's magnitude. There is no appreciable difference in t_c at 5° and 90°; the increase in t_c at 175° is likely due to saturation from hardware limitations, which occurs for steps larger than approximately 103° in our system. The best and worst case time responses for each magnitude are depicted in Fig. 6(b). It is worth noting that we did occasionally observe slip between the omniwheels at the magnet, which did not cause any problems in control.

2) Rotating Mode: The rotating mode was tested by selecting five axes to rotate the dipole moment around at three selected speeds (0.5, 1.5, and 2.5 Hz). The five axes were the $\hat{\mathbf{x}}$, $\hat{\mathbf{y}}$, and $\hat{\mathbf{z}}$ axes (see Fig. 2), and the omniwheel axes $\hat{\mathbf{a}}_1$ and $\hat{\mathbf{a}}_3$. (Note that $\hat{\mathbf{z}}$ and the omniwheel axis $\hat{\mathbf{a}}_2$ are parallel.) To evaluate the SAMM's ability to drive the dipole moment to the desired ro-

TABLE II
DIPOLE MOMENT WAS ROTATED ABOUT FIVE DISTINCT AXES FOR 30 S EACH

κ		x			y			z & $\mathbf{a}_2$			$\mathbf{a}_1$			$\mathbf{a}_3$		
$\omega_{\mathbf{m}}$ (Hz)		0.5	1.5	2.5	0.5	1.5	2.5	0.5	1.5	2.5	0.5	1.5	2.5	0.5	1.5	2.5
	$\epsilon_\perp$ (deg)	0.83	1.35	1.53	1.61	3.13	4.41	1.05	2.06	2.70	1.27	3.37	3.22	1.65	3.43	4.19
45°	t_s (sec)	0.28	0.41	0.41	0.26	0.20	0.25	0.30	0.57	0.46	0.37	0.61	0.41	0.32	0.60	0.40
	$\epsilon_{\boldsymbol{\kappa}}$ (Hz)	0.02	0.02	0.02	0.05	0.05	0.04	0.01	0.01	0.01	0.03	0.04	0.03	0.02	0.02	0.02
	$\epsilon_\perp$ (deg)	1.08	2.01	1.35	1.54	4.83	4.41	0.82	1.82	2.50	1.30	2.25	**2.65**	1.17	3.15	3.86
90°	t_s (sec)	0.38	0.43	0.38	0.38	0.26	0.50	0.36	0.25	0.26	0.33	0.65	**0.42**	0.43	0.43	0.31
	$\epsilon_{\boldsymbol{\kappa}}$ (Hz)	0.02	0.02	0.02	0.07	0.05	0.04	0.01	0.01	0.01	0.04	0.04	**0.03**	0.02	0.02	0.02

Note: $\epsilon_\perp$ is the RMS angular error from the desired plane and $\epsilon_{\boldsymbol{\kappa}}$ is the RMS angular velocity error during the last 15 s of rotation. The settling time (t_s) is defined as the time from rest to the dipole moment first crossing the desired plane. Bold response is shown in Fig. 7.
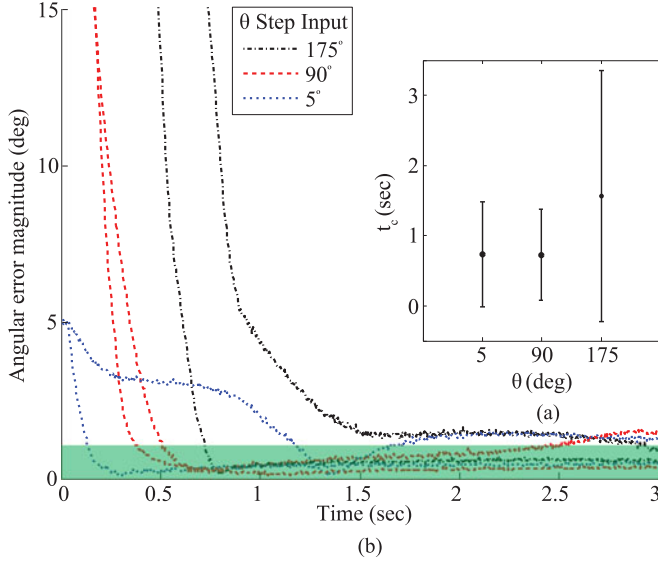

Fig. 6. (a) Inset shows the mean ± standard deviation of the convergence time to the desired heading with random changes in heading of angular magnitude θ. 50 trials were performed for each angular magnitude. (b) Best and worst case convergence time responses for each of the tested step-input magnitudes.
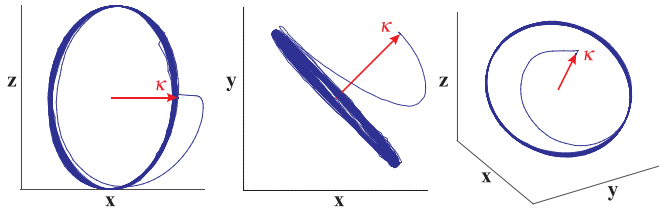

Fig. 7. Multiple views of a typical response using the rotating-mode controller with the dipole heading starting 90° off the desired plane and $\hat{\boldsymbol{\kappa}} = \hat{\mathbf{a}}_1$ at 2.5 Hz. The corresponding trial is bold in Table II.
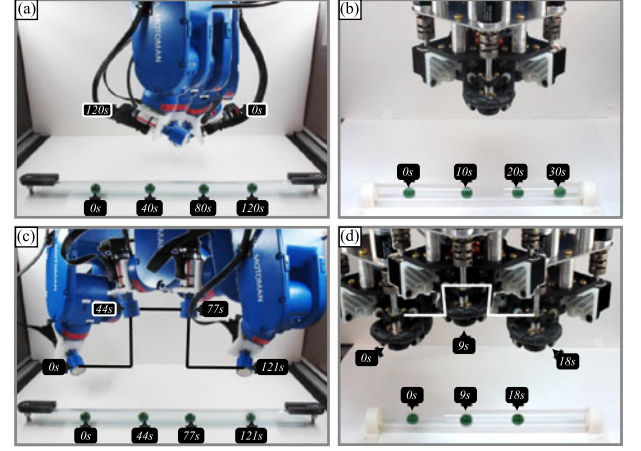

Fig. 8. (a) In prior work [1], a spherical UMD was rolled down a lumen using a rotating field generated by a permanent-magnet actuator, whose position was held stationary while its rotation axis was controlled appropriately. (b) For comparison, performing the same maneuver with the SAMM requires no motion of the robot manipulator. (c) In another example from [1], the UMD is rolled down a lumen while the permanent-magnet actuator's position follows a trajectory independent of the UMD's position while its rotation axis was controlled appropriately. (d) For comparison, when using the SAMM the manipulator's wrist only moves slightly to keep the SAMM in a constant orientation.

tation plane, the dipole moment was started with a heading of either 45° or 90° off the desired rotation plane. Table II gives the RMS error in angular error off the desired rotation plane ($\epsilon_\perp$), the time required to converge to the plane t_s, and the RMS error in angular speed ($\epsilon_{\boldsymbol{\kappa}}$). Note that $\epsilon_\perp$ and $\epsilon_{\boldsymbol{\kappa}}$ were both calculated from the last 15 s of each trial. Rotation axes do not perform identically across the workspace as illustrated in Table II due to nonlinearities and slight differences in the omniwheels. As expected, $\epsilon_\perp$ generally increases as the angular speed increases. Fig. 7 depicts a typical response with $\hat{\boldsymbol{\kappa}} = \hat{\mathbf{a}}_1$ at 2.5 Hz.

Next, we demonstrate the benefits of the SAMM relative to previous permanent-magnet actuation technology. In [1], we performed experiments where a spherical UMD was propelled down a lumen using a rotating field generated by a cylindrical permanent magnet as the UMD's position **p** was continuously measured by a stereo-camera system. The actuator magnet was rigidly attached orthogonally to the shaft of a DC motor, which was maneuvered in space by the same robotic manipulator used in this paper to control the magnet's rotation axis $\hat{\boldsymbol{\kappa}}$ according to

$$\hat{\boldsymbol{\kappa}} = \widehat{\mathbf{H}(\mathbf{p})\hat{\boldsymbol{\kappa}}_{\mathbf{h}}} \tag{36}$$

where $\hat{\boldsymbol{\kappa}}_{\mathrm{h}}$ is the instantaneous magnetic-field rotation axis that causes the UMD to roll down the lumen, and $\mathbf{H}(\mathbf{p}) = 3\hat{\mathbf{p}}\hat{\mathbf{p}}^\mathsf{T} - \mathbf{I}_3$ [1]. In one experiment, the UMD was rolled down the lumen while the Cartesian position of the actuator magnet was kept stationary [see Fig. 8(a)], which required the actuator-magnet's rotation axis, and thus the robot manipulator's wrist, to turn almost 180°. For comparison, Fig. 8(b) shows a similar experiment using the SAMM, but in this case the manipulator remains completely stationary. In a second experiment, the UMD was rolled down the lumen while the Cartesian position

of the actuator magnet followed a step trajectory independent of the UMD's position [see Fig. 8(c)], and the necessary actuator-magnet rotation axis from (36) caused the robot manipulator's wrist to contort dramatically (nearly violating joint limits at $t = 77$ s). For comparison, Fig. 8(d) shows a similar experiment performed with the SAMM. In this case, the manipulator's wrist remains nearly stationary throughout the trajectory, only changing slightly to keep the SAMM in a constant orientation. In both experiments, the SAMM dramatically reduces the manipulator motion required to perform the maneuvers. Note that both experiments were possible with the SAMM held in a constant orientation, demonstrating that a much simpler robot manipulator (e.g., a Cartesian gantry robot) could have been used to accomplish the same results.

IX. CONCLUSION

We have presented the spherical-actuator-magnet manipulator (SAMM), which is a singularity-free permanent-magnet robot end-effector for magnetic manipulation. The SAMM uses three omniwheels to enable holonomic control of a spherical magnet's heading and enable the magnet's rotation axis to be set arbitrarily. The SAMM performs closed-loop control of its magnet's heading using field measurements obtained from Hall-effect sensors as feedback, combined with modeled dynamics, using an extended Kalman filter. We experimentally characterized the quasi-static error in the estimate of the dipole's heading to be $1.5° \pm 0.6°$ (mean $\pm$ standard deviation). We described the operation and construction of the SAMM, developed and characterized pointing-mode and rotating-mode controllers, and demonstrated remote actuation of an untethered magnetic device in a lumen. Prior work in magnetic manipulation using permanent-magnet actuation was limited by robot joint limitations and singularities, but the SAMM end-effector substantially eliminates these limitations.

REFERENCES

[1] A. W. Mahoney and J. J. Abbott, "Generating rotating magnetic fields with a single permanent magnet for propulsion of untethered magnetic devices in a lumen," *IEEE Trans. Robot.*, vol. 30, no. 2, pp. 411–420, Apr. 2014.

[2] A. W. Mahoney and J. J. Abbott, "Five-degree-of-freedom manipulation of an untethered magnetic device in fluid using a single permanent magnet with application in stomach capsule endoscopy," *Int. J. Robot. Res.*, vol. 35, no. 1–3, pp. 129–147, 2016.

[3] B. J. Nelson, I. K. Kaliakatsos, and J. J. Abbott, "Microrobots for minimally invasive medicine," *Annu. Rev. Biomed. Eng.*, vol. 12, pp. 55–85, 2010.

[4] J. L. Toennies, G. Tortora, M. Simi, P. Valdastri, and R. J. Webster III, "Swallowable medical devices for diagnosis and surgery: the state of the art," *J. Mech. Eng. Sci.*, vol. 224, no. 7, pp. 1397–1414, 2010.

[5] G. Ciuti, P. Valdastri, A. Menciassi, and P. Dario, "Robotic magnetic steering and locomotion of capsule endoscope for diagnostic and surgical endoluminal procedures," *Robotica*, vol. 28, no. 2, pp. 199–207, 2010.

[6] M. T. Hou, H.-M. Shen, G.-L. Jiang, C.-N. Lu, I -J. Hsu, and J. A. Yeh, "A rolling locomotion method for untethered magnetic microrobots," *Appl. Phys. Lett.*, vol. 96, pp. 1–3, 2010, Art. no. 024102.

[7] S. Yim and M. Sitti, "Design and rolling locomotion of a magnetically actuated soft capsule endoscope," *IEEE Trans. Robot.*, vol. 28, no. 1, pp. 183–194, Feb. 2012.

[8] A. W. Mahoney and J. J. Abbott, "Managing magnetic force applied to a magnetic device by a rotating dipole field," *Appl. Phys. Lett.*, vol. 99, pp. 1–3, 2011, Art. no. 134103.

[9] J.-S. Lee, B. Kim, and Y.-S. Hong, "A flexible chain-based screw propeller for capsule endoscopes," *Int. J. Precis. Eng. Manuf.*, vol. 10, no. 4, pp. 27–34, 2009.

[10] L. Zhang, J. J. Abbott, L. X. Dong, B. E. Kratochvil, D. Bell, and B. J. Nelson, "Artificial bacterial flagella: Fabrication and magnetic control," *Appl. Phys. Lett.*, vol. 94, pp. 1–3, 2009, Art. no. 064107.

[11] K. Ishiyama, K. I. Arai, M. Sendoh, and A. Yamazaki, "Spiral-type micromachine for medical applications," *J. Micromechatronics*, vol. 2, no. 1, pp. 77–86, 2003.

[12] G. T. Gillies, R. C. Ritter, W. C. Broaddus, M. S. Grady, M. A. Howard III, and R. G. McNeil, "Magnetic manipulation instrumentation for medical physics research," *Rev. Sci. Instrum.*, vol. 65, no. 3, pp. 533–562, 1994.

[13] J. R. Clark, L. Leon, F. M. Warren, and J. J. Abbott, "Magnetic guidance of cochlear implants: Proof-of-concept and initial feasibility study," *J. Med. Devices*, vol. 6, 2012, Art. no. 035002.

[14] R. C. O'Handley, *Modern Magnetic Materials*. Hoboken, NJ, USA: Wiley, 2000.

[15] E. P. Furlani, *Permanent Magnet and Electromechanical Devices: Materials, Analysis, and Applications*. San Diego, CA, USA: Academic, 2001.

[16] M. Kumaga and T. Ochiai, "Development of a robot balanced on a ball: Application of passive motion to transport," in *Proc. IEEE Int. Conf. Robot. Autom.*, 2009, pp. 4106–4111.

[17] U. Nagarajan, G. Kantor, and R. Hollis, "The ballbot: An omnidirectional balancing mobile robot," *Int. J. Robot. Res.*, vol. 33, no. 6, pp. 917–930, 2014.

[18] M. Kumaga and R. L. Hollis, "Development of a three-dimensional ball rotation sensing system using optical mouse sensors," in *Proc. IEEE Int. Conf. Robot. Autom.*, 2011, pp. 5038–5043.

[19] L. Yan, I.-M. Chen, G. Yang, and K.-M. Lee, "Analytical and experimental investigation on the magnetic field and torque of a permanent magnet spherical actuator," *IEEE/ASME Trans. Mechatronics*, vol. 11, no. 4, pp. 409–419, Aug. 2006.

[20] S. E. Wright, A. W. Mahoney, K. M. Popek, and J. J. Abbott, "A spherical-magnet end-effector for robotic magnetic manipulation," in *Proc. IEEE Int. Conf. Robot. Autom.*, 2015, pp. 1190–1195.

[21] S. E. Wright, "A singularity-free mechanism for holonomic orientation control of a spherical permanent magnet," Master's thesis, Univ. Utah, Salt Lake City, UT, USA, 2014.

[22] H. Olsson, K. J. Åström, C. Canudas de Wit, M. Gäfvert, and P. Lischinsky, "Friction models and friction compensation," *Eur. J. Control*, vol. 4, no. 3, pp. 176–195, 1998.

[23] A. J. Petruska and J. J. Abbott, "Optimal permanent-magnet geometries for dipole field approximation," *IEEE Trans. Magn.*, vol. 49, no. 2, pp. 811–819, Feb. 2013.

[24] R. A. Horn and C. R. Johnson, *Matrix Analysis*, reprint ed. Cambridge, U.K.: Cambridge Univ. Press, 1985.

[25] D. Simon, *Optimal State Estimation*, 1st ed. Hoboken, NJ, USA: Wiley, 2006.

[26] T. W. R. Fountain, P. V. Kailat, and J. J. Abbott, "Wireless control of magnetic helical microrobots using a rotating-permanent-magnet manipulator," in *Proc. IEEE Int. Conf. Robot. Autom.*, 2010, pp. 576–581.

[27] A. Ghosh and P. Fischer, "Controlled propulsion of artificial magnetic nanostructured propellers," *Nano Lett.*, vol. 9, no. 6, pp. 2243–2245, 2009.

[28] M. Sendoh, K. Ishiyama, and K. I. Arai, "Fabrication of magnetic actuator for use in a capsule endoscope," *IEEE Trans. Magn.*, vol. 39, no. 5, pp. 3232–3234, Sep. 2003.

[29] K.-S. Byun and J.-B. Song, "Design and construction of continuous alternate wheels for an omnidirectional mobile robot," *J. Robot. Syst.*, vol. 20, no. 9, pp. 569–579, 2003.

[30] J. G. Ziegler and N. B. Nichols, "Optimum settings for automatic controllers," *Trans. ASME*, vol. 64, no. 11, pp. 759–768, 1942.

Samuel E. Wright received the B.S. and M.S. degrees in mechanical engineering from University of Utah, Salt Lake City, UT, USA, in 2012 and 2014, respectively.

After graduation, he was an Automation Engineer with Janicki Industries, Layton, UT, USA. He is currently with Sarcos Robotics, Salt Lake City, UT, USA.

Arthur W. Mahoney (S'10–M'15) received the B.S. degree in computer science from Utah State University, Logan, UT, USA, in 2009 and the Ph.D. degree in computing from University of Utah, Salt Lake City, UT, USA, in 2014.

He is a Postdoctoral Researcher with Vanderbilt University, Nashville, TN, USA.

Dr. Mahoney received an NSF IGERT Traineeship and an NSF Graduate Research Fellowship. He also received the Best Poster Award at the 2013 Hamlyn Symposium on Medical Robotics.

Jake J. Abbott (S'03–M'05) received the B.S. degree from Utah State University, Logan, UT, USA, in 1999; the M.S. degree from University of Utah, Salt Lake City, UT, USA, in 2001; and the Ph.D. degree from The Johns Hopkins University, Baltimore, MD, USA, in 2005, all in mechanical engineering.

In 2006, he became a Postdoctoral Researcher with ETH Zurich, Switzerland. In 2008, he joined the Department of Mechanical Engineering, University of Utah, where he is currently an Associate Professor.

Dr. Abbott is a recipient of the NSF CAREER Award. He also received the Best Manipulation Paper Award at the 2010 IEEE International Conference on Robotics and Automation, the Best Poster Award at the 2013 Hamlyn Symposium on Medical Robotics, and the Best Paper Award at the 2014 Haptics Symposium.

Katie M. Popek (S'06–M'16) received the B.S. degree in electrical engineering from University of Nebraska, Lincoln, NE, USA, in 2010 and the Ph.D. degree in computing from University of Utah, Salt Lake City, UT, USA, in 2017.

She is with The Johns Hopkins University Applied Physics Laboratory, Laurel, MD, USA.

Dr. Popek received an NSF IGERT Traineeship and an NSF Graduate Research Fellowship.